Thermal iodine release of surface implanted iodine in zirconia and its affect on hull disposal

F. Brossard, Noëlle Chevarier, Nathalie Moncoffre, Philippe Sainsot, Didier Crusset, Henri Jaffrezic

Thermal iodine release of surface-implanted iodine in zirconia and its affect on hull disposal

F. Brossard[a], N. Chevarier[a], N. Moncoffre[a,*], Ph. Sainsot[b], D. Crusset[c], H. Jaffrezic [d]

[a] *Institut de Physique Nucléaire de, Lyon, IN2P3/CNRS, Université Claude Bernard, 43, Bd du 11 Novembre 1918, F-69622 Villeurbanne cedex, France*

[b] *Institut National des Sciences Appliquées, UMR 5514, F-69621 Villeurbanne cedex, France*

[c] *ANDRA, Parc de la Croix Blanche, F-92298 Châtenay-Malabry cedex, France*

[d] *Ecole Centrale de Lyon, UMR 5621, F-69131 Ecully cedex, France*

During the reactor processing fission products, among which iodine is one, are implanted by recoil inside the Zir-caloy cladding tube, most of them being distributed within the first 2 μm. At the same time, oxidation of the cladding tubes occurs and therefore in the waste disposal phase zirconia will act as the first migration barrier. In order to analyse the mechanisms involved in iodine migration, stable and radioactive iodine atoms were introduced in oxidised zirco-nium samples by means of ion implantation at the near surface (mean range around 50 nm). Iodine thermal-release was measured either by Rutherford backscattering spectrometry (RBS) or γ-spectroscopy.

1. Introduction

The large uranium fission cross-section leads to long-lived fission products like iodine ^{129}I, and the behaviour of these elements in the cladding tube during energy production and afterwards during waste storage is a crucial problem [1,2]. During the reactor processing, fission products are implanted by recoil inside the Zir-caloy cladding tube at different energies ranging from keV to some tens of MeV, the larger fission product concentration being located at the very near surface [3–5], typically lower than 2 μm. Among fission products, iodine poses a real problem first since it is a volatile element and secondly because of the very long half-life of ^{129}I ($T = 1.59 \times 10^7$ yr). Two storage options are opened: the closed cycle in which wastes are reprocessed and the open cycle for which no reprocessing is performed. In the closed cycle, before fuel reprocessing, the cladding tubes taken apart from caps are sectioned into pieces called hulls. The hulls are collected as solid waste and in France they have been embedded inside a concrete structure since 1994. Presently, their compacting before storage is considered. In the perspective of geological disposal, a great interest is given to migration processes in order to model and to extrapolate them to large time scales [6,7]. We have undertaken this study on iodine migration into zirconia (zirconium oxide) since a natural oxidation of the internal face of the Zircaloy tube occurs during reactor processing simply by contact with the UO_2 fuel on a thickness ranging between 5 and 10 μm [5,8]. Hence most of the fission products are implanted in the first 2-μm superficial ZrO_2 layer. This work has been focused on migration phenomena occurring at the near zirconia surface (200 nm depth range), while previous studies [9,10] were devoted to deeper fission product implantation (around 1 μm depth range).

* Corresponding author. Tel.: +33-4 72 43 10 00; fax: +33-4 72 44 80 04.

E-mail address: moncof@ipnl.in2p3.fr (N. Moncoffre).

Table 1
Implantation parameters as a function of experimental implantation conditions

Iodine	Energy (keV)	R_p (nm)	σ (nm)	Implanted dose (ions cm^{-2})	C_m (at.%)
Radioactive	50	16	6	10^9	8×10^{-7}
Stable	50	16	6	8×10^{15}	3
Stable	200	46	16	8×10^{15}	1.8

Two implantation energies (50 and 200 keV) have been chosen. For each implantation condition, successive thermal air annealings were carried out. At each step of the annealing procedure, Rutherford backscattering spectrometry (RBS) was used in order to determine the iodine profiles corresponding to each annealing parameter (temperature, time). It allowed to analyse the migration process in terms of both the evolution of the iodine profiles and the mean iodine releases, and to get the signature of the involved mechanism. Complementary radioactive ion implantations involving doses less than 10^9 at. cm^{-2} were performed. In this case, the evolution of sample radioactivity was measured by γ-spectroscopy and analysed considering a diffusion process.

2. Experiment

This work was performed on reference samples obtained by the oxidation of pure polycrystalline zirconium foils (98.9%). At each step of this experimental procedure, analyses allowed to study the evolution of both the matrix and the implanted iodine.

2.1. Characterisation of the reference zirconia samples

The samples used in the experiments were obtained by annealing of pure polycrystalline zirconium under atmospheric pressure at 500°C for 3 h. The zirconia layer was characterised by Scanning electron microscopy (SEM) and RBS. SEM data obtained on a slant cut sample showed that the layer is homogeneous but the ZrO_2/Zr interface is not sharp [11]. These observations were confirmed by 3 and 7.5 MeV alpha backscattering measurements. The zirconia layer thickness deduced from RBS is 1.3 ± 0.2 μm, which is much larger than the implantation depth. Moreover a quite broad interface, around 0.3 μm thick, was observed. It is characteristic of the substoichiometric oxide growth at this interface.

2.2. Implantation and annealing conditions

These ZrO_2/Zr samples were implanted with 50 and 200 keV stable ^{127}I or 50 keV radioactive ^{131}I. The implantations were performed on the isotope separator of the 'Institut de Physique Nucléaire' of Lyon (IPNL). In case of 50 keV ^{131}I ion implantation, the ion source was fed with iodoethane labelled with ^{131}I which was obtained by isotopic exchange between iodoethane and a commercial sodium ^{131}I solution. The implanted dose was deduced from activity measurements, its order of magnitude was around 10^9 at. cm^{-2}. The implantation conditions are summarized in Table 1 together with the implantation parameters calculated from the SRIM (stopping and range of ions in matter) code [12]. For each implantation condition, thermal annealings were carried out in the 600–900°C temperature range. They were performed under air in a furnace allowing a continuous temperature regulation and an airflow control (60 ml min^{-1}). Such a thermal treatment induces both oxidation of the sample and the iodine migration. The oxidation kinetics was measured by thermogravimetry analysis and is presented in Fig. 1. It is first described by a parabolic rate law, which changes to a linear rate as a function of time. These results are characteristic of the zirconium corrosion in air [13] and water [14,15]. Such a transition between the parabolic and the linear kinetics is known to be correlated to a distortion of the lattice and that is why the post transition oxide is usually called porous zirconia while the pre-transition oxide is called compact zirconia. In this work, the annealing times were set such as to avoid the oxidation transition and to allow the study of iodine diffusion in compact zirconia only.

2.3. RBS results

The profiles deduced from RBS with 2 and 3 MeV He^+ particles, for the 50 and 200 keV implantations,

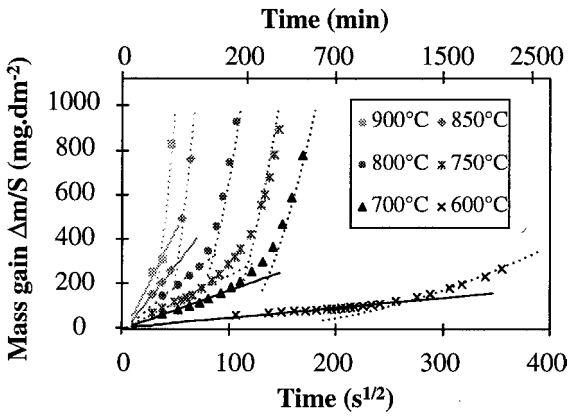

Fig. 1. Oxidation kinetics of zirconium between 600°C and 900°C measured by thermogravimetry analysis.

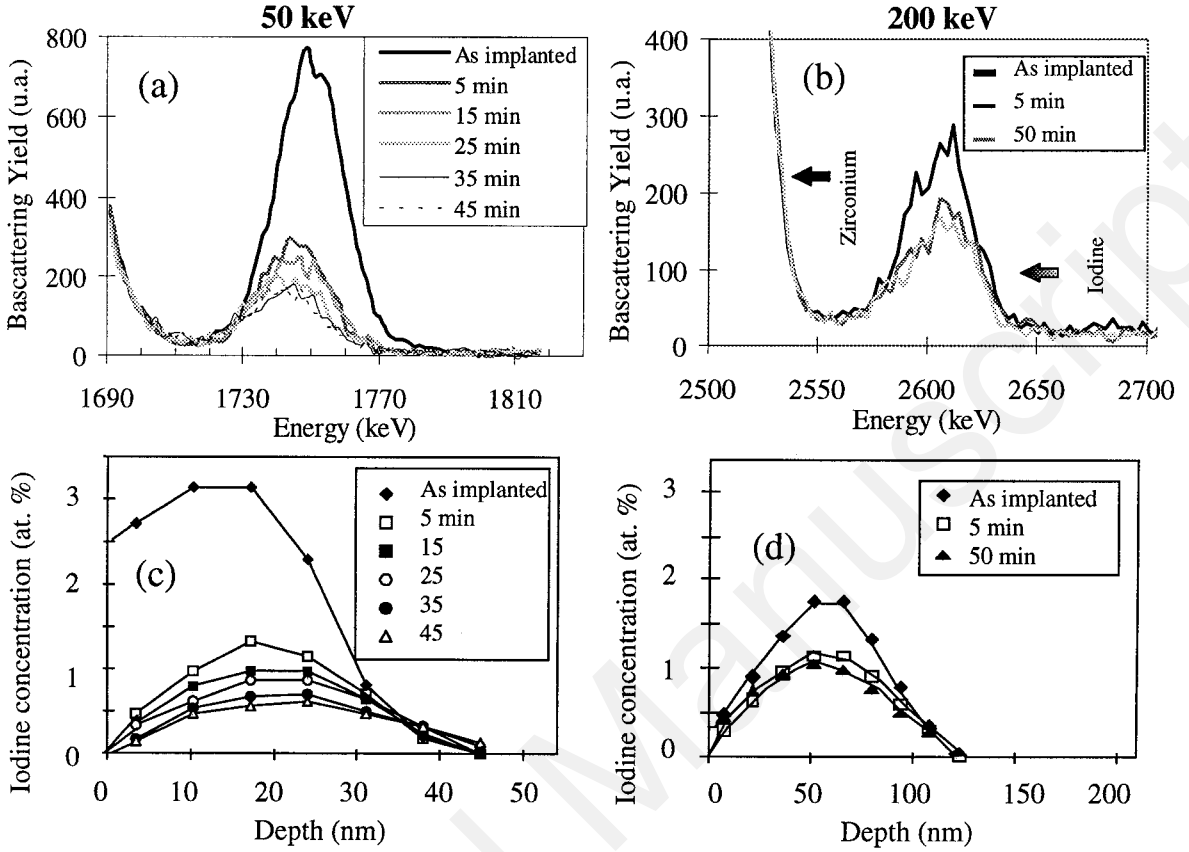

Fig. 2. Experimental RBS profile evolution (a, b) and deduced concentration profile evolution (c, d) of stable iodine implanted at 50 and 200 keV during successive annealings at 900°C.

respectively and after successive 900°C annealing steps are given in Fig. 2. Iodine distribution profiles (Fig. 2(c) and (d)) are deduced from energetic distributions of α backscattered particles (Fig. 2(a) and (b)) using a classical RBS simulation programme. Dots represent mean calculated values on depths ranging between 5 and 12 nm. In the case of 50 keV implantation, because of the surface etching, the iodine concentration at the surface

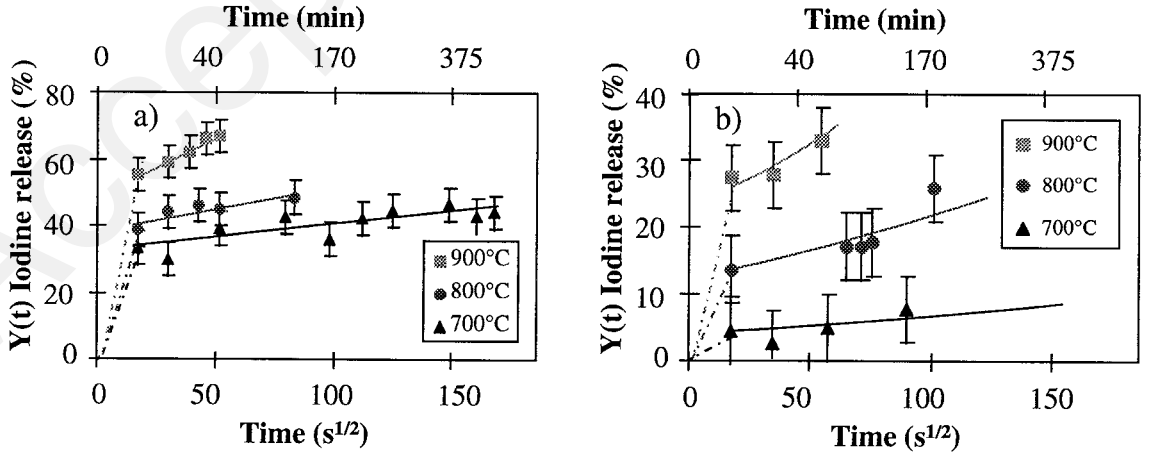

Fig. 3. Iodine release evolution of stable iodine implanted at 50 keV (a) and 200 keV (b) for different annealing temperatures. Full lines represent the simulation of iodine release.

in the as-implanted sample is nearly 3% (Fig. 2(c)). A strong iodine release larger than 55% is observed after 5 min annealing. After this rapid release, a much slower evolution occurs which can be related to a diffusion process. In the case of the deeper implantation at 200 keV (Fig. 2(d)), the surface concentration is lower and the rapid release yield decreases significantly.

Such a feature is clearly indicated in Fig. 3(a) and (b), where the iodine release evolution is presented at various temperatures as a function of the square-root of time. This representation allows to distinguish two different release mechanisms as suggested by Matzke [16]. The release rate $Y(t)$ is obtained by integration of the profiles for each annealing condition taking the implanted dose as a reference. Let us denote $N(0)$, the total iodine concentration deduced from the integration of RBS profiles in the as-implanted sample and $N(t)$, the iodine concentration measured after an annealing time t.

Hence

$$Y(t) = \frac{N(0) - N(t)}{N(0)}.$$

Whatever the implantation energy, a rapid decrease is observed at the beginning of the annealing experiments. It is always followed by the diffusion phase. Let us first focus on this diffusion phase.

3. Diffusion coefficient measurement using stable iodine implantation

In this section, the mechanisms involved in iodine migration are studied analysing both the evolution of concentration profiles and the iodine release rate as a function of annealing conditions. Let us analyse in more detail the 50 keV data in order to take into account only the diffusion phase. These experimental data represent measurements performed beyond 5 min annealings as shown in Fig. 4(a). This figure shows the evolution of the iodine depth profile during annealing at 900°C. A slight broadening of the distributions as well as a small iodine release occur with increasing time. No shift of the distributions can be observed within the experimental resolution of the technique (around 10 nm). The data are interpreted on the basis of a diffusion model derived from Fick's second law.

3.1. Description of the fitting procedure

In this section, the mechanisms involved in iodine migration are studied analysing both the evolution of concentration profiles and the iodine release rate as a function of annealing conditions. Let us analyse in more details the 50 keV data. These experimental data concern measurements performed beyond 5 min annealing as shown in Fig. 4(a). The data are interpreted on the basis of a diffusion model derived from Fick's second law.

In a previous paper [17], we proposed an analytical approach which is valid in the case of large release rate only. In this work, a numerical analysis has been performed.

According to Fick's second law

$$\frac{\partial C(x,t)}{\partial t} = D\frac{\partial^2 C(x,t)}{\partial x^2}, \tag{1}$$

where C is the concentration of the diffusing species and D is the diffusion coefficient. Solutions vary depending on initial and boundary conditions. In order to avoid the rapid release rate, the initial condition is taken after 5 min of annealing time. We have assumed that at time $t = 0$, the concentration profile exhibits a gaussian shape

$$C(x, t=0) = C_m \exp\left(\frac{-(x - R_p)^2}{2\sigma^2}\right), \tag{2}$$

where R_p is the projected implantation range, σ the straggling and C_m is the iodine concentration at $x = R_p$.

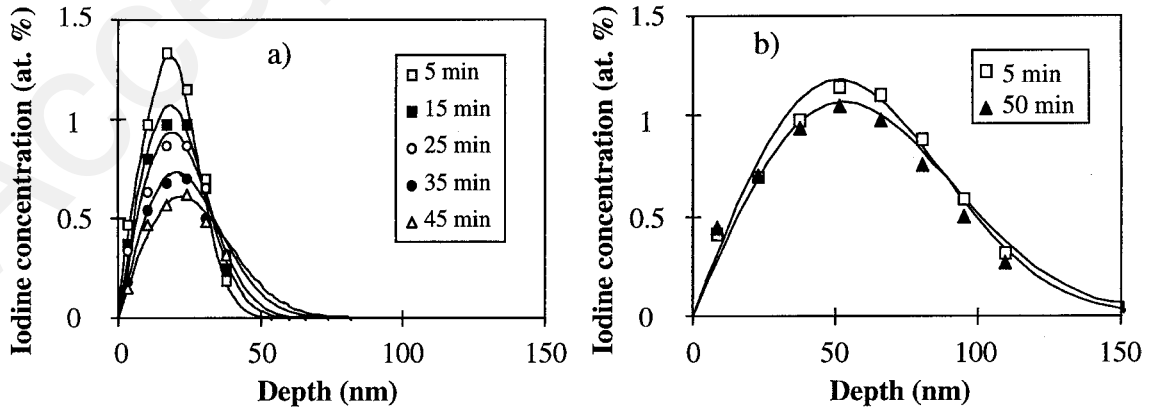

Fig. 4. Simulation of the diffusion profiles at 900°C of stable iodine implanted at 50 keV (a) and 200 keV (b).

Concerning the boundary conditions, within the RBS resolution, the iodine concentrations at the surface and far from the surface remain equal to zero whatever the annealing time. These results have been confirmed by X-ray photoelectron spectroscopy experiments, which show that already after a 5 min annealing, the iodine surface contribution observed on the as-implanted sample disappears. From these experimental considerations: $C(0,t)=0$ and $C(\infty,t)=0$.

Let us rewrite Fick's second law with dimensionless variables

$$\bar{x}=\frac{x}{\sigma},\quad \bar{C}=\frac{C}{C_m},\quad \text{therefore : } \frac{\partial^2\bar{C}}{\partial\bar{x}^2}=\frac{\sigma^2}{D}\frac{\partial\bar{C}}{\partial t},$$

$$\text{If } \bar{t}=\frac{tD}{\sigma},\quad \text{then } \frac{\partial^2\bar{C}}{\partial\bar{x}}=\frac{\partial\bar{C}}{\partial\bar{t}}.$$

The integration is performed using the finite difference method with an explicit scheme

$$\frac{\partial^2\bar{C}}{\partial\bar{x}^2}=\frac{\bar{C}_{i+1}^n-2\bar{C}_i^n+\bar{C}_{i-1}^n}{\Delta\bar{x}^2}\quad\text{and}\quad\frac{\partial\bar{C}}{\partial\bar{t}}=\frac{\bar{C}_i^{n+1}-\bar{C}_i^n}{\Delta\bar{t}},$$

i and n corresponding, respectively, to the discretisation of depth and time. Therefore

$$\bar{C}_i^{n+1}=(1-2r)\bar{C}_i^n+r\left(\bar{C}_{i+1}^n+\bar{C}_{i-1}^n\right),$$

where $r=\Delta\bar{t}/\Delta\bar{x}^2$ is taken lower than 0.5 to ensure the stability of the scheme.

Starting from the initial distribution profile after 5 min annealing, the diffusion is numerically simulated. In order to determine the diffusion coefficient D, we search for the time $\bar{t}$ required to fit correctly the iodine release after an annealing time t. We deduce

$$D=\frac{\bar{t}}{t}\sigma^2.$$

3.2. Diffusion coefficient extraction from experimental data

The fits obtained at 900°C using such a numerical approach are given by full lines in Fig. 4(a) and (b) for 50 and 200 keV implantations, respectively. They show clearly that the experimental data are well described by the simulations. The fits performed at each annealing step allow one to deduce a mean diffusion coefficient value corresponding to a specific temperature. We notice that such an analysis allows one to reproduce the iodine release evolution. As shown in Fig. 3, there is a good agreement between the experimental points and the simulation data represented by full lines for each temperature. Both the analyses lead to apparent diffusion coefficient values nearly equal within the uncertainty limits. Therefore, the average values have been determined and they are given in Table 2 together with the uncertainty limits.

Table 2
Diffusion coefficients of stable iodine in zirconia and the related uncertainties (ΔD)

Temperature (°C)	D (cm^2 s^{-1})	ΔD (cm^2 s^{-1})
900	56.5×10^{-17}	13×10^{-17}
800	19.5×10^{-17}	5×10^{-17}
700	4×10^{-17}	2×10^{-17}

4. Analysis of the two release phases using radioactive iodine implantation

4.1. Diffusion coefficient determination in the slow release phase.

The iodine release $Y(t)$ was deduced from activity measurements at each step of the annealing procedure by gamma spectroscopy ($E_\gamma=364$ keV). The activity $A(0)$ of the as-implanted sample was taken as reference. $A(t)$ corrected for the radioactivity decrease was the residual activity of the sample after an annealing time t which leads to the desorption rate $Y(t)$

$$Y(t)=\frac{A(0)-A(t)}{A(0)}.$$

The high sensitivity of the radioactive tracer technique allows measurements down to a temperature of 600°C. The iodine releases observed from 600°C to 900°C annealing temperatures on 50 keV implanted samples are given in Fig. 5. A much lower iodine release yield is generally noticed in the first 5 min compared to the results obtained with stable species. Before analysing in

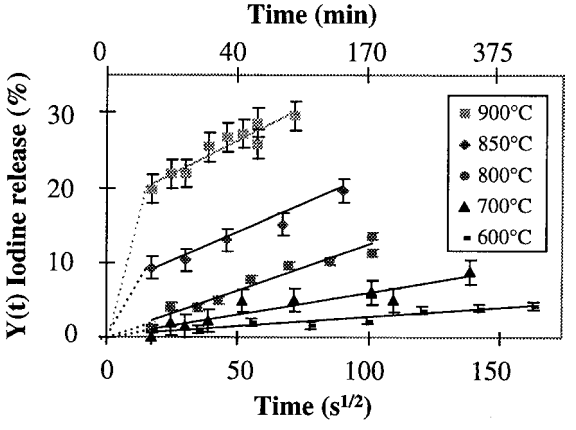

Fig. 5. Evolution of radioactive iodine release $Y(t)$ vs time for different temperatures.

Table 3
Diffusion coefficients of radioactive iodine in zirconia and the related uncertainties (ΔD)

Temperature (°C)	D (cm^2 s^{-1})	ΔD (cm^2 s^{-1})
900	8.5×10^{-17}	1.5×10^{-17}
850	5.0×10^{-17}	0.8×10^{-17}
800	5.8×10^{-17}	0.7×10^{-17}
700	1.9×10^{-17}	0.6×10^{-17}
600	0.36×10^{-17}	0.1×10^{-17}

more detail, this rapid surface desorption, let us determine the diffusion coefficients in the slow phase.

Since in that case it is not possible to determine experimentally the initial profile, we have made the hypothesis that they fit well to the profile given by the SRIM code. In addition, the implanted dose being very low (10^9 ions cm^{-2}), we have assumed that the surface etching can be neglected. The numerical procedure is the same as described above. Results of the numerical simulations are presented in Fig. 5 (full lines). Table 3 gives the diffusion coefficients deduced at each temperature. They are systematically lower than those of stable iodine. This difference is more noticeable for the highest temperatures. The much smaller error bar at 700°C in the case of the radioactive species is mainly due to the experimental technique itself.

4.2. Analysis of the rapid iodine surface desorption

We have shown that the rapid desorption depends on the surface concentration since at 200 keV implantation the iodine release was lower than at 50 keV. Based on these experimental data, we have made the hypothesis that the iodine release yield in the first 5 min was correlated to iodine surface concentration and to the defects created by irradiation too [18]. However, as shown in Fig. 5, a 20% iodine release is observed at 900°C in case of radioactive implantation while the surface concentration is 10^8 smaller and the defect rate is negligible. It is then obvious that iodine release dependence on iodine surface concentration is not linear.

In a first step, we have studied the influence of irradiation defects. Zirconia layer samples have been first irradiated with 800 keV energy bismuth ions at different doses ranging from 5×10^{14} to 5×10^{15} at. cm^{-2}. Such irradiations induce defects, which were estimated around 5–50 displacements per atom (dpa). Radioactive iodine ^{131}I was then introduced in the so-obtained sample by ion implantation at 50 keV energy. The iodine implantation dose was fixed to 8×10^9 at. cm^{-2} corresponding to 5×10^{-6} dpa, which are much lower than defect rates due to bismuth irradiation. Energies have been chosen in order to avoid the overlap between bismuth and iodine distributions. Bismuth and iodine profiles deduced from SRIM-96 code calculation are

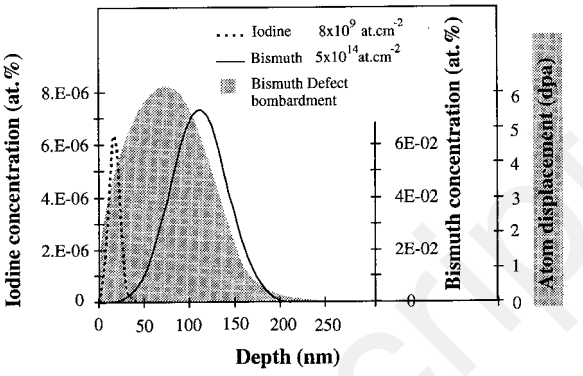

Fig. 6. Iodine and bismuth depth distributions. The dark zone corresponds to the defect depth profile created by a 5×10^{14} at. cm^{-2} bismuth irradiation dose.

displayed in Fig. 6. It must be noticed that the iodine distribution is located in the near surface part of the defect distribution due to bismuth bombardment. The characterisation of both iodine release and zirconia structure evolution related to bismuth irradiation was performed.

The iodine release results are presented in Fig. 7, which puts into evidence the fact that the rapid desorption phase in the first 5 min of annealing depends on the bismuth dose going through a maximum value at 5×10^{14} Bi cm^{-2}, while the slower diffusion process is independent on the irradiation dose. Moreover, measurements by grazing angle X-ray diffraction (GAXRD) were performed at a 0.8° grazing angle, which allows to analyse a zirconia layer depth of 200 nm [19,20]. This corresponds to the bismuth depth profile. The X-ray diffraction spectra are very different depending on the various bismuth doses (Fig. 8). Globally, the monoclinic contribution decreases in favour of the tetragonal one when the bismuth dose increases. Using the Garvie and Nicholson formula [21,22], we have determined the apparent proportion $X(t)$ of the tetragonal structure in the oxide film

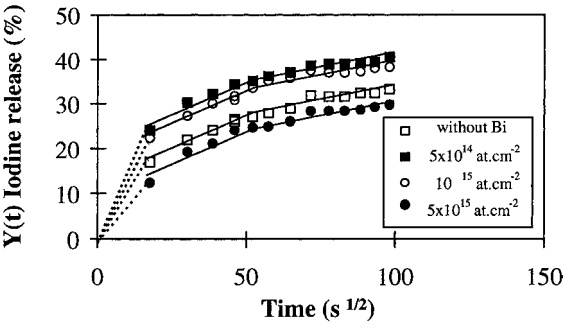

Fig. 7. Iodine release at 800°C vs the square root of time for different bismuth irradiation doses.

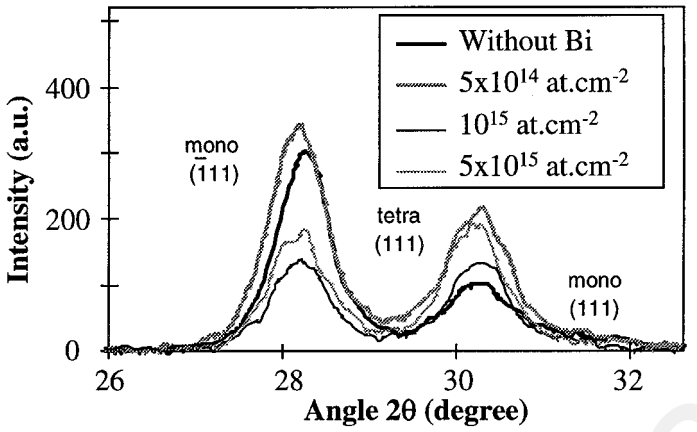

Fig. 8. X-ray diffraction spectra of a non-irradiated sample and Bi irradiated samples.

$$X(t) = \frac{I(\bar{1}\,1\,1)_t}{I(\bar{1}\,1\,1)_m + I(1\,1\,1)_m + I(\bar{1}\,1\,1)_t},$$

where $I(\bar{1}\,1\,1)_t$ is the intensity of the $(\bar{1}\,1\,1)_t$ ray of tetragonal zirconia ($2\theta = 30.2°$), $I(\bar{1}\,1\,1)_m$ the intensity of the $(\bar{1}\,1\,1)_m$ ray of monoclinic zirconia ($2\theta = 28.2°$) and $I(1\,1\,1)_m$ is the intensity of the $(1\,1\,1)_m$ ray of monoclinic zirconia ($2\theta = 31.5°$).

The evolution of the rapid iodine release versus the bismuth dose is presented in Fig. 9 together with the evolution of the zirconia structure. An increase of the iodine release from a non-irradiated sample to a sample irradiated at 5×10^{14} at. cm^{-2} is noticed. In the case of higher bismuth doses, no more release enhancement is observed. A similar evolution is observed concerning the zirconia structure. Initially, one can notice an increase of the tetragonal zirconia proportion from 20% (non-irradiated sample) to 50% (irradiation dose 10^{15} at. cm^{-2}), then later a saturation effect occurs when higher bismuth doses are involved. It must be added that in this experiment, the delay time between iodine implantation and iodine release measurement was set for each sample as equal to 26 h. Such a caution was necessary in order to make these data reliable since the delay time is a sensitive parameter of the quick release at the beginning of the analysis.

In a second step, we have studied the influence of the delay time. During this time interval, the samples were stored at room temperature. It is important to

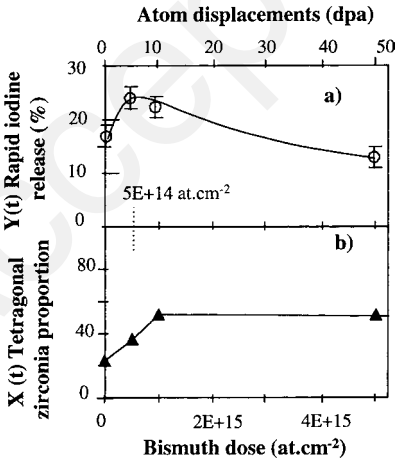

Fig. 9. Iodine release after 5 min annealing (a) and Evolution of the tetragonal zirconia proportion (b), vs the bismuth irradiation dose.

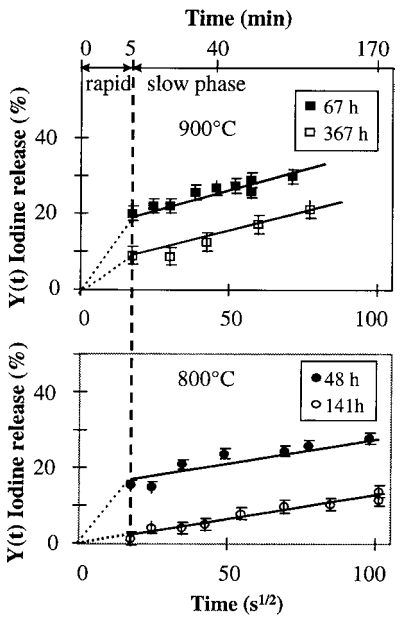

Fig. 10. Comparison of radioactive iodine release for short and long delay times at 800°C and 900°C.

emphasize that in this condition, no iodine release could be observed. In order to put into evidence the influence of the delay time on iodine migration, we performed the 800°C and 900°C annealing and the iodine measurements on samples corresponding, respectively, to short (around 2 d) and long (around 10 d) delay times. Results are illustrated in Fig. 10. It is clearly seen that for both temperatures in the rapid phase, the iodine release decreases when the delay times increases. However, in the slow phase, the diffusion coefficients are independent of this delay time as shown by the simulation data (full lines) that remain parallel for all the delay times.

5. Discussion

Whatever the experimental conditions (energy, dose), two iodine release phases have been observed: a rapid desorption and a slow diffusion phase. In the case of stable iodine, diffusion coefficients are nearly the same for both energies. From the Arrhenius law, it was possible to determine an activation energy for iodine diffusion in zirconia of 1.1 ± 0.3 eV at.$^{-1}$. The Arrhenius diagram is shown in Fig. 11. In the case of radioactive species, the diffusion coefficients are systematically lower but remain of the same order of magnitude. The activation energy is found to be 1.0 ± 0.1 eV at.$^{-1}$. These activation energy values are relatively low. This could be explained by the presence of stoichiometric vacancies in compact zirconia as suggested by Chien and Heuer [23].

The rapid release phase was shown to depend on the bismuth irradiation dose and on the crystallisation of tetragonal zirconia. We have also demonstrated that the impact of the delay time was of major importance on the rapid desorption phase. By extrapolation for very long delay times, this rapid phase would disappear. It seems to indicate that a reorganisation of the zirconia structure occurs at room temperature under air. This ageing phenomenon was already mentioned [24,25]. From these authors, H_2O adsorption from the surface could favour a material transformation. They put in evidence that the proportion of monoclinic phase was dependent on ageing. Both diffusion and annealing of vacancies could be a consequence of this ageing phenomenon. In our study, at 600°C and up to 900°C annealing temperatures, zirconia is recovering during the first 5 min of annealing corresponding to the rapid phase, while stoichiometric vacancies persist, this is related to the low activation energy during the iodine diffusion process.

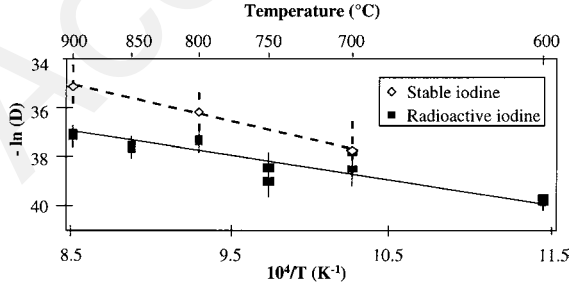

Fig. 11. Arrhenius diagram of stable and radioactive iodine diffusion in zirconia.

Since the rapid desorption tends to disappear as a function of time for very low iodine concentrations, it can be assumed in the context of nuclear waste disposal that the slow diffusion process is the only determining one. An extrapolation to storage temperature conditions (around 50°C) leads to a diffusivity inferior to 10^{-26} cm^2 s^{-1}. Nevertheless, this value does not take into account the irradiation effects and the dissolution effects due to the surrounding medium (like water). Such studies are now carried out [26].

Acknowledgements

The authors would like to thank A. Plantier who performed the implantations and A. Chevarier who performed the isotopic exchange.

References

[1] V.M. Oversby, Mater. Sci. Technol. B 10 (1994) 392.
[2] R.C. Ewing, W.J. Weber, F.W. Clinard, Prog. Nucl. Energy 29 (2) (1995) 63.
[3] T. Hirabayashi, T. Sato, C.N. Sagawa, M. Masaki, M. Saeki, T. Adachi, J. Nucl. Mater. 45 (1990) 174.
[4] M. Fregonese, thesis, Institut National Polytechnique of Grenoble, France, October 1997.
[5] R. Restani, E.T. Aerne, G. Bart, H.P. Linder, A. Müller, F. Petrik, Technical Report 92-13, Nagra, Wettingen, Switzerland, 1992.
[6] D.J. Cherniak, W.A. Lanford, F.J. Ryerson, Nucl. Instrum. and Meth. B 45 (1990) 230.
[7] Hj. Matzke, Nucl. Instrum. and Meth. B 32 (1988) 453.
[8] H. Kleykamp, J. Nucl. Mater. 171 (1990) 181.
[9] N. Moncoffre, A. Chevarier, N. Chevarier, N. Millard-Pinard, in: T. Von Egidy, D. Habs, F.J. Hartmann, K.E.G. Lübner, H. Niefnecker (Eds.), International Workshop on Research with Fission Fragments, World Scientific, Singapore, 1997, p. 287.
[10] F. Brossard, A. Chevarier, N. Chevarier, N. Moncoffre, D. Crusset, H. Faust, P. Sainsot, Proceedings of the Seventh International Conference on Radioactive Wastes Management and Environmental Remediation, Nagoya, Japan, September 1999.
[11] F. Brossard, thesis, Université C. Bernard, Lyon-1, France, September 1999.
[12] J.P Biersack, L.G. Haggmark, Nucl. Instrum. and Meth. 174 (1980) 257.
[13] V.B. Voitovich, V.A. Lavrenko, R.F. Voitovich, E.I. Golovko, Oxidation of Metals 42 (1994) 223.

[14] International Atomic Energy Agency, Waterside corrosion of zirconium alloys in nuclear power plants, IAEA-TECDOC-996, IAEA, Vienna, 1998.
[15] C. Lemaignan, A.T. Motta, Mater. Sci. Technol. B 10 (1994).
[16] Hj. Matzke, Radiat. Eff. 53 (1980) 219.
[17] N. Chevarier, F. Brossard, A. Chevarier, D. Crusset, N. Moncoffre, Nucl. Instrum. and Meth. B 136–138 (1998) 784.
[18] K.E. Sickafus, Hj. Matzke, K. Yasuda, P. Chodak, R.A. Verral, P.G. Lucuta, H.R. Andrews, A. Turos, R. Fromknecht, N.P. Baker, Nucl. Instrum. and Meth. B 141 (1998) 358.
[19] M. Brunel, J. Phys. (Paris) IV, Colloq. 6 (4) (1996) 321.
[20] E.F. Keable, in: E. F. Kaeble (Ed.), Handbook of X-rays, 1967.
[21] R.C. Garvie, P.J. Nicholson, J. Am. Ceram. Soc. 55 (6) (1972) 303.
[22] P. Barberis, J. Nucl. Mater. 226 (1995) 34.
[23] F.R. Chien, A.H. Heuer, Philos. Mag. 73 (1996) 681.
[24] Dae-Joon Kim, J. Euro. Ceram. Soc. 17 (1997) 897.
[25] Xin Guo, J. Phys. Chem. 60 (1999) 539.
[26] K. Poulard, A. Chevarier, N. Moncoffre, Nucl. Instrum. and Meth. B, to be published.